Research article

Unraveling the structural complexity of and the effect of calcination temperature on calcium phosphates derived from *Oreochromis niloticus* bones

Tanachat Eknapakul [a], Arreerat Jiamprasertboon [a], Penphitcha Amonpattaratkit [b,c], Adulphan Pimsawat [d], Sujittra Daengsakul [d], Nantawat Tanapongpisit [e], Wittawat Saenrang [e], Atipong Bootchanont [f,g], Pattarapong Wannapraphai [h,i], Thanawat Phetrattanarangsi [h,i], Thanachai Boonchuduang [h], Atchara Khamkongkaeo [i,j,*], Rattikorn Yimnirun [k]

[a] Functional Materials and Nanotechnology Center of Excellence, School of Science, Walailak University, Nakhon Si Thammarat, 80160, Thailand
[b] Synchrotron Light Research Institute (Public Organization), Muang, Nakhon Ratchasima, 30000, Thailand
[c] Biodyne Co., Ltd, Seoul, 04793, Republic of Korea
[d] Department of Physics, Faculty of Science, Khon Kaen University, Khon Kaen, 40002, Thailand
[e] School of Physics, Institute of Science, Suranaree University of Technology, Nakhon Ratchasima, 30000, Thailand
[f] Smart Materials Research Unit, Division of Physics, Faculty of Science and Technology, Rajamangala University of Technology Thanyaburi, Pathumthani, 12110, Thailand
[g] Division of Physics, Faculty of Science and Technology, Rajamangala University of Technology, Thanyaburi, Pathumthani, 12110, Thailand
[h] Biomechanics Research Center, Meticuly Co. Ltd., Chulalongkorn University, Bangkok, 10330, Thailand
[i] Department of Metallurgical Engineering, Faculty of Engineering, Chulalongkorn University, Phayathai Road, Wangmai, Pathumwan, Bangkok, 10330, Thailand
[j] Center of Excellence in Biomaterial Engineering in Medical and Health, Faculty of Engineering, Chulalongkorn University, Bangkok, Thailand
[k] School of Energy Science and Engineering, Vidyasirimedhi Institute of Science and Technology VISTEC, Wangchan, Rayong, 21210, Thailand

ARTICLE INFO

ABSTRACT

In this study, the interplay between the structural complexity, microstructure, and mechanical properties of calcium phosphates (CaPs) derived from fish bones, prepared at various calcination temperatures, and their corresponding sintered ceramics was explored. Fourier-transform infrared analysis revealed that the calcined powders primarily consisted of hydroxyapatite (HAp) and carbonated calcium hydroxyapatite, with an increasing concentration of Mg-substituted β-tricalcium phosphate (β-TCP) as the calcination temperature was increased. X-ray diffraction patterns showed enhanced sharpness of the peaks at higher temperatures, indicating a larger crystallite size and improved crystallinity. The ceramics exhibited a significantly larger crystallite size and an increased concentration of the β-TCP phase. Rietveld analysis revealed a larger volume of the β-TCP phase in the ceramics than in their calcined powders; this could be attributed to a newly formed β-TCP phase due to the decomposition of HAp. Extended X-ray absorption fine structure analysis revealed the incorporation of Mg in the Ca2 site of HAp, Ca2 site of β-TCP, and Ca5 site of β-TCP, with a higher substitution of Mg in the Ca5 site of β-TCP at elevated temperatures. The mechanical properties of HAp ceramics can be improved by

* Corresponding author Department of Metallurgical Engineering, Faculty of Engineering, Chulalongkorn University, Phayathai Road, Wangmai, Pathumwan, Bangkok, 10330, Thailand.
 E-mail address: atchara.k@gmail.com (A. Khamkongkaeo).

increasing the calcination temperature because of their improved relative density and dense porous structure at elevated temperatures. This comprehensive investigation sheds light on the phase evolution, microstructural changes, and consequential impact on the mechanical properties of CaPs derived from fish bones, thereby facilitating the development of tailored CaP ceramics for biomedical applications.

1. Introduction

Calcium phosphate (CaP) is a predominant mineral commonly found in the form of hydroxyapatite (HAp) [$Ca_{10}(PO_4)_6(OH)_2$], and it plays a crucial role in the hardness and strength of living bones and teeth [1,2]. Owing to its structural similarity to the human bone and chemical stability, HAp has been extensively investigated for applications in bone regeneration and medical implants [3,4]. However, the brittleness of HAp limits its application as a load-bearing implant [5]. Researchers have aimed to enhance the mechanical properties of HAp by modifying its physical characteristics and incorporating impurity ions (doping) or preparing composites [6,7]. Ramesh et al. [8] demonstrated that HAp samples sintered at 1250 °C exhibited improved mechanical properties, which were correlated with the relative density and grain growth of the sintered samples. Previous studies have shown that the mechanical characteristics of ion-doped nano-HAp/chitosan composites are significantly influenced by their preferred growth orientation [7]. Heat treatment can produce biphasic calcium phosphate, a mixture of HAp and β-tricalcium phosphate (β-TCP), via the decomposition of HAp, which strongly affects the mechanical properties of the material [9–11]. The β-to α-TCP phase transition, which impedes grain formation, occurs at temperatures greater than 1125 °C and significantly influences the mechanical characteristics of the material [12–14]. Notably, doping with Mg can hinder this phase transformation and maintain a uniform particle distribution, leading to increased relative density and enhanced mechanical properties of CaPs [15,16].

CaPs can be obtained from various natural sources such as fish bones, bovine bones, and poultry eggshells [17–19]. Naturally derived HAp has received significant attention owing to its cost-effective and environmentally friendly production. Additionally, these naturally derived CaPs exhibit improved immunogenic responses because they closely resemble the physicochemical properties of authentic bone apatite [20]. The properties of naturally extracted CaPs are diverse and influenced by factors such as structural composition, trace elements, and organic compounds [8,21]. Living bones typically comprise approximately 70 % HAp, with 3–8% comprising carbonated calcium hydroxyapatite (CHAp) [11]. CHAp can be categorized as A-type (with CO_3^{2-} ions substituting the OH^- sites) or B-type (with CO_3^{2-} ions substituting the PO_4^{3-} sites) [22]. Unlike in pure HAp, the presence of CO_3^{2-} ions in the lattice of bone minerals alters their mechanical properties [23,24]. The remaining portion of the bone mineral can exist in the rhombohedral structure with the *R3c* space group, such as whitlockite {$Ca_9Mg(PO_4)_6[PO_3(OH)]$}, merrillite [$Ca_9NaMg(PO_4)_7$], or β-TCP [$Ca_3(PO_4)_2$], depending on the presence of trace elements and functional groups [25]. Experimentally, HAp and CHAp can be distinguished based on the presence of CO_3^{2-} absorption bands in the Fourier-transform infrared (FTIR) spectra [22]. Each *R3c* phase can be identified by the presence of HPO_4^{2-} absorption bands in the FTIR spectra and shifts in X-ray diffraction (XRD) peaks resulting from changes in the chemical bonds or lattice parameters due to the substitution of alkali and alkaline earth metals [2,21].

A wide range of calcium to phosphorus (Ca/P) ratios, approximately 1.3–1.9, can be observed in different natural specimens [22, 26]. CaPs derived from natural bones can alter the HAp to β-TCP ratio, and the degree of crystallinity and crystallite size can be enhanced at higher calcination temperatures [27,28]. Goto and Sasaki observed that fish bones with a high Mg content contained less crystalline HAp and exhibited a greater formation of β-TCP compared with other types of fish bones [4]. Additionally, our recent research showed that HAp derived from fish bones possesses better mechanical properties than chemically synthesized HAp owing to its increased grain size [17].

The mechanical properties of CaPs obtained from natural sources are significantly influenced by their structural complexity, which is higher than those of the synthesized powders. A thorough examination using scanning electron microscopy (SEM), XRD, and FTIR spectroscopy can offer valuable insights into the microstructural features and phase composition, capturing the intricate details of the hierarchical structure of CaPs derived from natural sources. By conducting a comprehensive analysis of the structural complexity of CaPs, researchers can uncover the interplay between these factors and develop a deeper understanding on CaP mechanical properties. Thus, CaPs derived from natural sources should be comprehensively analyzed because they possess greater structural complexity than their synthesized counterparts.

2. Experimental section

2.1. Preparation of the powders and ceramic samples

In this study, HAp powders were derived from the bones of Nile tilapia (*Oreochromis niloticus*), and the extraction process is detailed in a previous study [17]. Tilapia bone fragments were calcined at 600, 700, 800, and 900 °C at a heating rate of 5 °C/min for 2 h under an air atmosphere. The calcined bone fragments were then allowed to cool naturally in an electric furnace (SX2-4-17 TP, XINKYO, China). Subsequently, the resultant products were ground using an electric herb grinder for 10 min, yielding biogenic HAp powders designated as P_600, P_700, P_800, and P_900. For the morphological, Vickers hardness, and compression tests, ceramic samples were fabricated by employing the methodology outlined in our previous study [17]. All samples were subjected to sintering at 1250 °C at a heating rate of 5 °C/min for 3 h under an air atmosphere. The sintered ceramics (C_600, C_700, C_800, and C_900) were allowed to cool

naturally within the furnace. This experiment aimed to maintain the sintering temperature constant in order to focus solely on the effect of the calcination temperature.

2.2. Characterization methods

The elemental compositions of all powders were assessed by performing X-ray fluorescence (XRF) spectrometry (S8 TIGER, Bruker, USA). FTIR analysis (TENSOR 27, Bruker, USA) was performed in the wavenumber range of 4000–600 cm^{-1} to investigate the functional groups present in both powders and ceramics. The phase structures of the powders and ceramics were determined using XRD (Bruker D2 Phaser diffractometer, USA). High-quality XRD patterns were recorded at 25 °C in the 2θ scanning range of 20°–80° at an increment of 0.02°/step and a step time of 2 s. Rietveld refinement was performed using the TOPAS software. The relative density of all ceramic samples was calculated using the Archimedes method. Additionally, the surface morphologies of the ceramic samples were examined using field-emission SEM (Quanta 250 FEG, Czech Republic).

EXAFS measurements were conducted in the fluorescence-yield mode on the BL8: X-ray absorption spectroscopy beamline at the Synchrotron Light Research Institute. The sample was mounted on a polyimide tape and placed on the EXAFS sample holder. Spectra were recorded at 25 °C in the photon (X-ray) energy range (Mg K-edge). Photon energies were scanned using a Beryl (101 $\bar{0}$) double crystal monochromator and calibrated against the K-edge of Mg metal (1303 eV) using a Mg foil. The monochromatic X-ray beam size was 15 mm × 1 mm, and the X-ray attenuation length was approximately 0.5 μm for the scanned X-ray energies. Normalization procedures were performed using the Athena software (Demeter System, Version 0.9.26) [25].

To assess the mechanical properties of the ceramic samples, Vickers hardness tests were conducted using a diamond indenter with a load of 200 gf on a MVK-H2 microhardness tester (Mitutoyo, Japan). Compression tests were performed at room temperature using an AGS-X 100 kN compression tester (Shimadzu, Japan) at a strain rate of 0.01/min. Ten data points for Vickers hardness tests and five data points for compressive strength tests were recorded for each sample.

2.3. Computational methodology

The optimized crystal structure calculations for Mg-doped HAp and Mg-doped β-TCP were performed by using first-principles density functional theory implemented in the Vienna ab initio simulation package codes [29], employing projector-augmented plane-wave pseudopotentials [30]. Fully relaxed calculations were performed by using the generalized gradient approximation exchange-correlation functional with the Perdew–Burke–Ernzerhof functional [31]. For Mg-doped HAp, a plane-wave cut-off of 520 eV was used for the calculations. The Brillouin zone was sampled by employing Monkhorst–Pack grids with 5 × 5 × 5 k-point meshes [32]. The Mg-doped HAp system comprised 44 atoms (1 Mg atom, 9 Ca atoms, 6 P atoms, and 28 O atoms). For Mg-doped β-TCP, crystal structures with Mg substitution at the Ca1, Ca2, Ca3, Ca4, or Ca5 sites of β-TCP were initially obtained. A collective Mg-doped β-TCP system consisted of 276 atoms (1 Mg atom, 65 Ca atoms, 42 P atoms, and 168 O atoms). The optimized crystal structure was obtained with a 500 eV energy cutoff and a Monkhorst–Pack scheme grid with a 1 × 1 × 1 mesh of k-points. A relaxation convergence criterion for all self-consistent iterations was achieved when the total energy and force difference between the cycles were below 0.001 meV/atom and 0.01 meV/Å, respectively. The Mg K-edge EXAFS profiles of Mg-doped HAp and Mg-doped β-TCP were evaluated using the FEFF9 codes [33]. The FEFF code utilizes a full multiple-scattering approach based on ab initio overlapping muffin-tin potentials. The muffin-tin potentials for self-consistent calculations are used in FEFF codes with the Hedin–Lundqvist exchange-correlation function within a spherical radius of 5.0 Å [34]. The full multiple-scattering calculations for all possible paths were performed within a larger cluster radius of 8.0 Å.

Table 1
Elemental compositions of all calcined powders determined by performing XRF analysis.

Element	Amount (at.%)			
	P_600	P_700	P_800	P_900
Ca	35.14	34.88	34.53	34.86
P	20.39	20.16	20.23	20.38
Mg	1.02	0.97	0.98	0.97
Na	1.07	1.06	1.28	1.06
K	0.14	0.17	0.16	0.10
S	0.17	0.15	0.16	0.16
Cl	0.08	0.07	0.05	0.06
Sr	0.03	0.03	0.03	0.03
Zn	0.02	0.02	0.01	0.01
Fe	0.03	–	0.01	0.01
Light elements (i.e. O and H)	Balanced	Balanced	Balanced	Balanced
Ca/P ratio	1.723	1.730	1.707	1.711

3. Results and discussion

3.1. Elemental composition of the calcined powders

The elemental compositions of the calcined powders, as determined by conducting XRF analysis, are presented in Table 1. The dominant elements in all the powders are Ca and P, with trace amounts of Mg, Na, K, S, Cl, Sr, Zn, and Fe, whereas O and H account for the remaining composition. Mg and Na are the most abundant in all the calcined powders. The inclusion of Mg in CaP has been shown to significantly impact the crystallinity of HAp, leading to the formation of a more stable β-TCP [4,15]. The Ca/P ratios of the powders are determined to be approximately 1.707–1.730, slightly higher than the stoichiometric value of 1.67 for HAp. The Ca/P ratio can vary between 1.58 and 1.79 depending on the type of animal bone and preparation conditions [29]. The higher Ca/P ratio observed in this study may be influenced by residual raw components (CaO), the formation of $CaO-P_2O_5$ complexes, and carbonate apatite [22,29, 30]. Notably, the elemental composition exhibits insignificant changes during calcination at different temperatures.

3.2. FTIR analysis of the calcined powders

The FTIR spectra of the calcined powders in the wavenumber range of 4000–600 cm^{-1} are presented in Fig. 1. All powders exhibit characteristic OH^- absorption bands at approximately 3572 and 630 cm^{-1} and bands corresponding to PO_4^{3-} at 1087, 1020, and 962 cm^{-1}; both groups are indicative of HAp [35]. Several CO_3^{2-} vibration peaks at approximately 1450 and 880 cm^{-1} [36] suggest that residual carbonates in the calcined powders are commonly observed in CaPs derived from natural sources [21,35]. At higher temperatures, doublet absorption bands of PO_4^{3-} are observed at approximately 982 and 947 cm^{-1}, displaying a shift of approximately 5 cm^{-1} toward higher wavenumbers, similar to those reported for β-TCP [37,38]. This shift is consistent with previous findings indicating the incorporation of Mg in the β-TCP structure (β-MgTCP) [2]. The intensity of these PO_4^{3-} bands increase with the temperature, indicating a higher β-MgTCP content in the samples.

The P_600 and P_700 powders exhibit absorption bands corresponding to CO_3^{2-} at 874, 1412, and 1463 cm^{-1} (blue dashed lines), whereas these bands shift to 883, 1423, and 1481 cm^{-1} (red dashed lines) for the P_800 and P_900 samples. The observed CO_3^{2-} bands correspond to carbonate substitution at the hydroxyl (A-CHAp) and phosphate (B-CHAp) sites. Typically, absorption bands at 1530, 1465, and 879 cm^{-1} represent A-CHAp, whereas those at 1456, 1423, and 872 cm^{-1} represent B-CHAp [39]. Our samples possibly include both A- and B-type carbonates. In typical bone minerals, the carbonate is primarily of the B type because of the smaller size of the phosphate site [4,39]. The shift of CO_3^{2-} bands may be influenced by either the promotion of the A-CHAp phase via a high energy input or changes in the chemical bonds due to an increase in β-MgTCP within the structure. No HPO_4^{2-} absorption bands (doublet peaks at 917 and 860 cm^{-1}) are observed for any of the powders, suggesting that whitlockite may have already lost its HPO_4^{2-} group and transformed into other CaPs via heat treatment [2,40].

3.3. XRD analysis of the calcined powders

Fig. 2(a–d) displays the XRD patterns of the calcined powders at room temperature. The observed Bragg reflections match well with the patterns indexed as HAp (JCPDS No. 01-072-1243) with minor amounts of the β-TCP phase (JCPDS No. 01-070-2065), and no other impurities are detected. As the calcination temperature increases, sharper XRD peaks are observed without the appearance of new phases. This finding is consistent with those of previous studies demonstrating a transition from broad to sharp XRD peaks in different precursors, indicating improved crystallinity and crystallite size with an increasing operating temperature [18,41,42]. Rietveld refinement was performed to analyze various parameters, including the phase composition, crystallite size, and lattice constants. Table 2 presents the results, revealing an increase in the crystallite size from tens to a few hundred nanometers and the presence of 15.7–20.3 % β-TCP phase in the powders calcined at high temperatures. The lattice parameters of HAp show minor variations, with a ≈9.42 Å and c ≈ 6.88 Å, which is consistent with previous report [43]. However, the lattice constants of the β-TCP phase are slightly lower than those of the chemically pure β-TCP [44]. Because of the presence of Mg and Na in the samples, the β-TCP phase can represent minerals in the *R3c* space group, such as whitlockite, merrillite, or β-MgTCP, which are estimated to account for approximately 20 % of the inorganic components of living bones based on the amount of Mg^{2+} [2]. Small deviations in the peak positions resulting from the differences in the lattice constants and functional groups can aid in distinguishing the *R3c* phases [2]. The highest
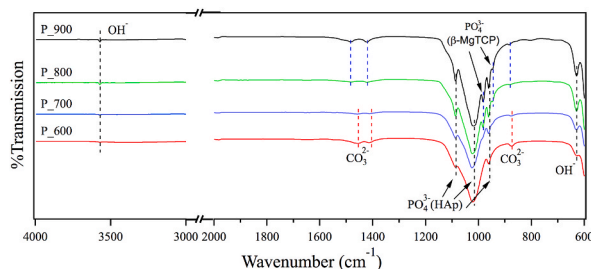
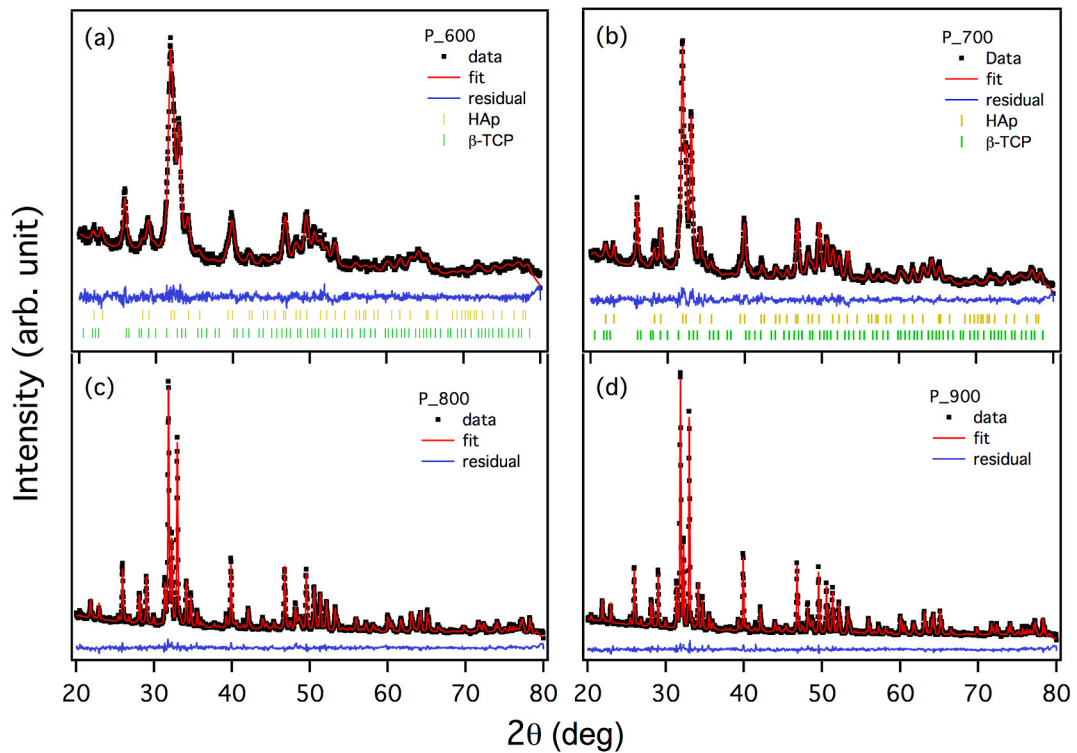

Fig. 1. FTIR spectra of the calcined powders.

Fig. 2. XRD patterns and Rietveld refinement plots of powders calcined at various temperatures: (a) 600 °C (P_600), (b) 700 °C (P_700), (c) 800 °C (P_800), and (d) 900 °C (P_900), with a heating rate of 5 °C/min for 2 h under an air atmosphere.

Table 2
Refined parameters of the calcined powders.

| Parameter	P_600	P_700	P_800	P_900
HAp (%)	84.30(31)	79.70(13)	82.68(52)	80.80(52)
Crystallite size, HAp (nm)	22.5(16)	38.4(15)	133.4(39)	265.0(13)
a, HAp (Å)	9.4086(42)	9.4236(28)	9.4208(30)	9.4204(15)
c, HAp (Å)	6.8749(32)	6.8835(21)	6.8817(28)	6.8831(17)
vol., HAp (Å³)	527.050(53)	529.390(35)	528.940(40)	528.998(22)
β-TCP (%)	15.70(31)	20.30(13)	17.32(52)	19.20(52)
Crystallite size, β-TCP (nm)	11.4(18)	18.4(20)	142.0(18)	159.0(17)
a, β-TCP (Å)	10.3640(15)	10.3658(50)	10.3493(70)	10.3586(53)
c, β-TCP (Å)	36.8210(59)	36.8580(23)	37.0459(40)	37.0664(30)
vol., β-TCP (Å³)	3425.00(11)	3429.80(39)	3436.36(60)	3444.44(45)
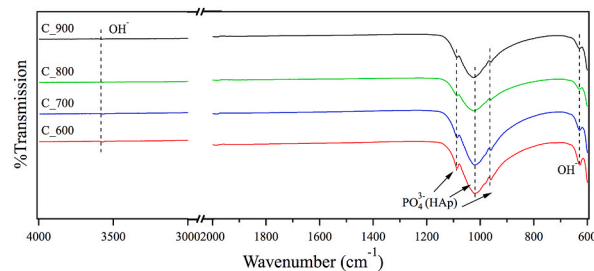
Fig. 3. FTIR spectra of the sintered ceramics.

R3c peak is observed at 31.39°, which is higher than those observed for β-TCP but close to those observed for β-MgTCP [45,46]. This shift to a higher angle suggests lattice contraction due to the incorporation of Mg into the structure [47]. Analysis of the FTIR spectra indicates the absence of HPO_4^{2-} absorption bands, which are characteristic of whitlockite and supports the exclusion of this phase. Additionally, no significant shift in the peaks of the HAp phase is observed, suggesting that the structural deformations or phase transitions between A-type and B-type CHAp during calcination are negligible [39,48].

3.4. FTIR analysis of the sintered ceramics

Fig. 3 presents the FTIR spectra of the sintered ceramics, which show remarkable similarity. Some prominent peaks are the OH^- adsorption bands observed at approximately 3572 and 630 cm^{-1} and the PO_4^{3-} bands at 1087, 1020, and 962 cm^{-1}. Notably, the absence of CO_3^{2-} bands in the spectra suggests the breakdown of CHAp and other associated carbonates, indicating the successful removal of contaminants during sintering. Additionally, a decrease in the OH^- vibrational intensities and broadening of the PO_4^{3-} bands in the FTIR spectra of the ceramics, particularly in the range of 1200–900 cm^{-1}, indirectly indicate the incorporation of Mg into the sample structure [49].

3.5. XRD analysis of the sintered ceramics

Fig. 4(a–d) depicts the XRD patterns of the sintered ceramics, and Table 3 lists the refined parameters. All ceramics exhibit sharper XRD patterns than their corresponding calcined powders without additional phases. The HAp phase in all ceramics exhibits calculated crystallite sizes ranging from 615 to 957 nm, whereas the β-TCP phase displays sizes approximately half of those of the HAp phase. The concentration of the β-TCP phase in the C_600, C_700, C_800, and C_900 ceramics is determined to be 24.74(49)%, 24.59(55)%, 31.30(55)%, and 27.16(60)%, respectively. These concentrations are notably higher than those in the corresponding powders, indicating the decomposition of HAp into the β-TCP phase at these temperatures [50]. Slight variations in the lattice parameters and volume are observed for both the HAp and β-TCP phases in the sintered ceramics. However, a larger volume of the β-TCP phase is observed in them than in their corresponding powders; this could be attributed to the newly generated β-TCP phase, where the ionic radius of Ca^{2+} is considerably larger than that of Mg^{2+}. Consequently, the increased presence of the *R3c* phase in the sintered ceramics is possibly
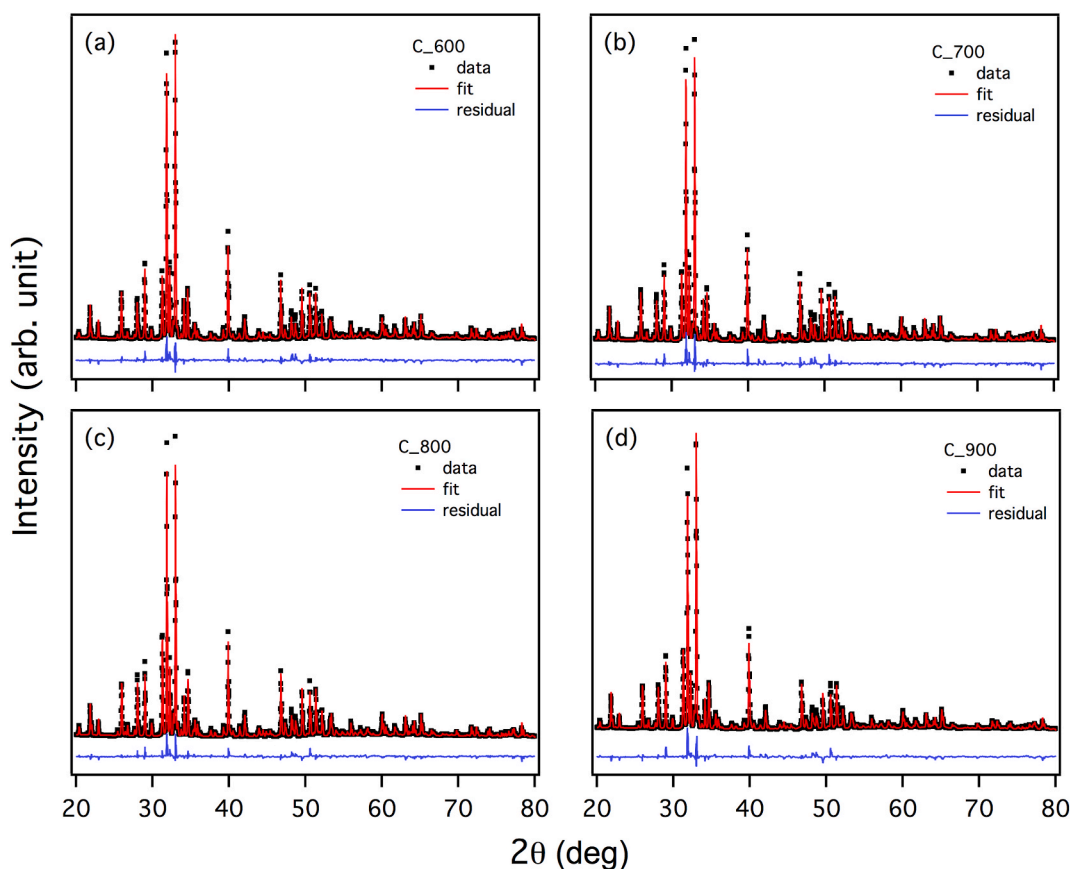

Fig. 4. XRD patterns and Rietveld refinement plots of sintered ceramics, prepared at 1250 °C for 3 h with a heating rate of 5 °C/min under an air atmosphere, using powders calcined at various temperatures: (a) 600 °C (C_600), (b) 700 °C (C_700), (c) 800 °C (C_800), and (d) 900 °C (C_900).

Table 3
Refined parameters of the sintered ceramics.

Parameter	C_600	C_700	C_800	C_900
HAp (%)	75.26(49)	75.41(55)	68.70(55)	72.84(60)
Crystallite size, HAp (nm)	615(49)	673(60)	957(82)	738(60)
a, HAp (Å)	9.4147(11)	9.4136(11)	9.4163(12)	9.4166(19)
c, HAp (Å)	6.8817(13)	6.8806(13)	6.8817(12)	6.8817(19)
vol., HAp (Å^3)	528.260(16)	528.052(15)	528.441(17)	528.476(26)
β-TCP (%)	24.74(49)	24.59(55)	31.30(55)	27.16(60)
Crystallite size, β-TCP (nm)	278(22)	287(24)	520(54)	374(45)
a, β-TCP (Å)	10.3773(28)	10.3764(27)	10.3714(23)	10.3687(36)
c, β-TCP (Å)	37.1252(17)	37.1235(15)	37.1589(12)	37.1692(20)
vol., β-TCP (Å^3)	3462.36(25)	3461.60(23)	3461.57(19)	3460.70(30)

because of the β-MgTCP and β-TCP phases resulting from HAp decomposition.

3.6. EXAFS analysis of the sintered ceramics

EXAFS is an essential technique for investigating the local structure and identifying trace elements and doping in HAp, which significantly influence HAp properties. The EXAFS profiles of all calcined powders and sintered ceramics are presented in Fig. 5(a). The EXAFS profiles of the calcined powders show significant smearing, possibly owing to their low crystallinity [51]. However, distinct spectral patterns are observed for the powders calcined at higher temperatures, indicating improved crystallinity. In the sintered ceramics, the spectral patterns are more distinct, indicating a high degree of crystallinity and phase transformation. To analyze these spectral patterns, the simulated X-ray absorption near-edge structure (XANES) profiles of Mg-substituted Ca1 and Ca2 in HAp (Ca1H and Ca2H) and Ca1 to Ca5 in β-TCP (Ca1β to Ca5β) are examined, as shown in Fig. 5(b). The positions and intensities of peaks A, B, and C resemble those of the Ca2H and Ca2β spectra, whereas peak D is characteristic of the Ca5β structure. A Ca2H:Ca2β:Ca5β ratio of 30:40:30 is obtained by employing linear combination fitting on the C_900 ceramic. This finding contradicts those of previous studies that reported Mg substitution in the Ca4 and Ca5 sites of the β-TCP structure [17]. This suggests that the local structure of Mg can be altered by using different sources or preparation methods. Notably, the intensity of peak D increases with an increasing calcination temperature in both powders and ceramics, indicating a greater substitution of Mg in the Ca5β site in samples calcined at higher temperatures. This observation is consistent with the increased β-TCP content reported in the XRD results. The changes in the EXAFS profiles of the sintered ceramics indicate that the calcination temperature influences the local structure. This phenomenon can be ascribed to the required activation energy combined with the operating temperature and time required to overcome the energy barrier
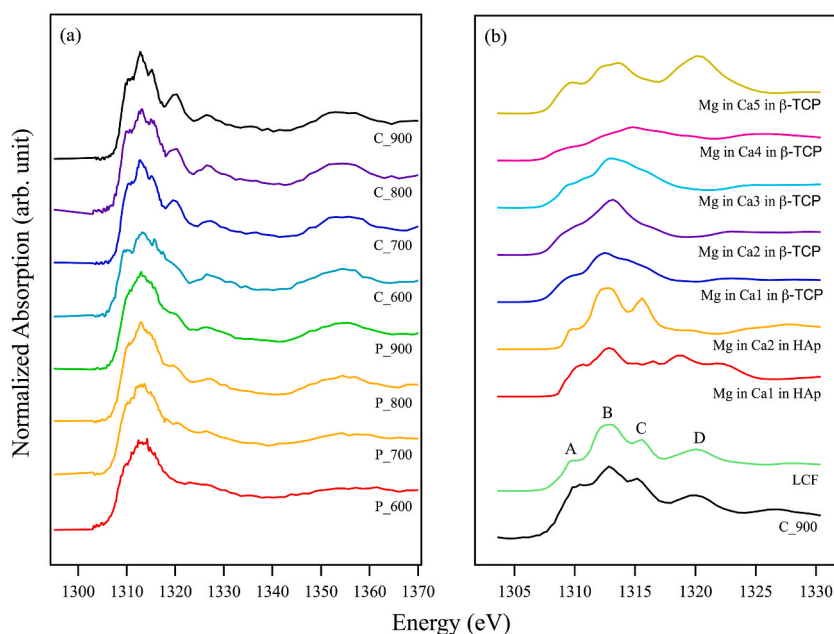

Fig. 5. (a) EXAFS profiles of the calcined HAp powders and sintered ceramics and (b) simulated XANES profiles of Mg-substituted HAp and β-TCP; XANES profile of the C_900 ceramic and its linear combination fitting.

for the formation of new crystalline phases.

3.7. Morphology of the sintered ceramics

Fig. 6(a–d) shows SEM images of the sintered ceramics without surface polishing. The micrographs demonstrate the presence of densely packed and interconnected grains, with an average grain size of approximately 3.5 ± 0.6 μm observed across all samples. A few pores are noticeable on the surface of the C_600 ceramic, but their presence diminishes as the calcination temperature increases (see Fig. 6(a)). The inset highlights the internal crack morphologies of the ceramics synthesized at different calcination temperatures. In particular, the C_600 ceramic exhibits small loosely bound agglomerated particles, resulting in internal pores and fractures. In contrast, ceramics subjected to higher calcination temperatures display a more compact structure with reduced pore content. Notably, the C_900 sample exhibits a well-packed morphology with minimal residual porosity as shown in Fig. 6(d).

The relative density is measured to be 84.51 ± 2.12 %, 87.49 ± 1.03 %, 85.70 ± 1.66 %, and 91.48 ± 0.97 % for the C_600, C_700, C_800, and C_900 ceramics, respectively. These findings are consistent with the observed morphological characteristics and apparent porosities of the samples. Notably, the relative density of HAp ceramics can vary owing to several factors, including the particle size, particle size distribution, specific surface area, densification, grain growth, and composition of the ceramic material [8,17]. Our results suggest that the development of internal grains significantly influences ceramics produced at different calcination temperatures. Furthermore, the calcination process induces porosity formation, variations in the pore size, fracture formation, phase transformation, and changes in the crystallinity of the sintered ceramics. The presence of pores in the samples can be attributed to the removal of residual components from the compacted powders.

3.8. Mechanical properties of the sintered ceramics

Fig. 7(a and b) illustrates the compressive strength (C_s) and Vickers hardness (V_h) of the sintered ceramics obtained at different calcination temperatures. The sample sizes of the sintered ceramics used for the compression tests are listed in Table 4. The C_s values are determined to be 13.58 ± 2.92, 29.26 ± 1.40, 39.88 ± 4.44, and 54.37 ± 7.61 MPa, whereas the V_h values are found to be 0.46 ± 0.09, 0.58 ± 0.05, 2.00 ± 0.30, and 2.92 ± 0.37 GPa for the C_600, C_700, C_800, and C_900 ceramics, respectively. Based on the values of mean $\pm$ standard deviation, differences in the mechanical properties of the samples can be observed, except for the Vickers hardness of the C_600 and C_700 samples. The mechanical properties of the sintered ceramics exhibit a consistent upward trend with an increasing calcination temperature. The mechanical properties of HAp are typically influenced by factors such as phase concentration, grain size, density, and porosity [6–8]. However, the interplay between these factors can be complicated, and further research is required to understand their contributions.

Our analysis revealed slight variations, and no clear trend, in grain size (3.5 ± 0.6 μm), the crystallite size (ranging from 600 to 900
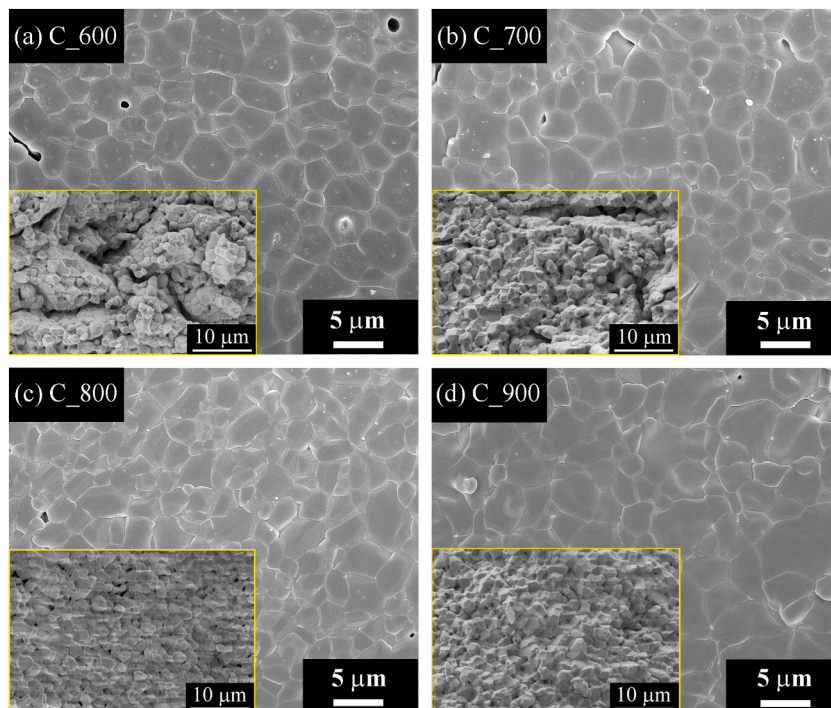

Fig. 6. (a)–(d) SEM micrographs of the sintered ceramics at different temperatures. Insets show the SEM images of the internal cracks.
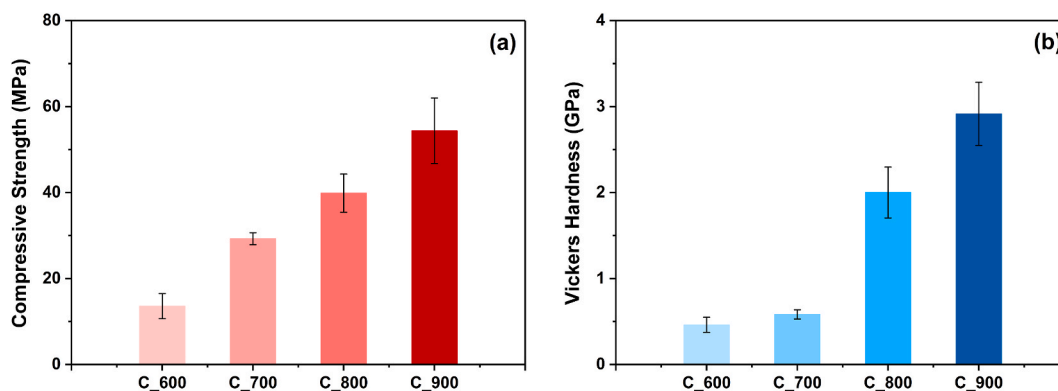
Fig. 7. (a) Compressive strength and (b) Vickers hardness of all sintered ceramics.

Table 4
Sample sizes of the sintered ceramics for compression tests.

Sample	No.	Diameter (mm)	Height (mm)
C_600	1	12.20	17.83
	2	12.07	20.03
	3	12.05	23.01
	4	12.01	19.97
	5	12.21	21.76
C_700	1	12.39	19.20
	2	12.27	18.69
	3	12.33	17.10
	4	12.45	19.01
	5	12.30	16.99
C_800	1	13.02	19.40
	2	13.03	18.37
	3	13.04	22.99
	4	13.01	20.61
	5	13.06	18.01
C_900	1	13.02	21.44
	2	13.04	21.76
	3	13.06	21.48
	4	13.03	21.62
	5	13.04	20.96

nm for HAp and 278–520 nm for β-TCP), and the composition of β-TCP (ranging from 24.74 % to 31.30 %) across all samples, as expected from the same sintering temperature. One might expect that these similarities would result in comparable mechanical properties. However, our research uncovered an upward trend in mechanical properties, contrary to typical expectations. Our results indicate that ceramics sintered at the same temperature but calcined at different temperatures exhibit lower porosity and higher relative density as a function of calcining temperature. Then, the observed enhancement in mechanical properties can primarily be attributed to the lower porosity and higher relative density of the sintered ceramics calcined at higher temperatures. Furthermore, we found that the effect of grain size, crystallite size, and phase composition may be too small compared to the effect of porosity and relative density on the observed mechanical properties. Additionally, our XRD and EXAFS findings indicate significant phase transitions and crystallization during the sintering process. These results suggest that samples with a higher substitution of Mg in the Ca5 site of β-TCP may exhibit improved mechanical properties. It is plausible to propose that samples with initially low crystallinity may hinder grain growth and the formation of well-ordered crystallites, thereby resulting in poorer mechanical properties at the microscopic level.

The range of our observed mechanical properties is indeed suitable for dental and trabecular bone replacement applications. In the study by Chun et al. [52], which reports the compressive strength, Vickers hardness, and roles of enamel and dentin in human teeth, our observed mechanical properties closely aligned with their report, suggesting that these values are suitable for enamel and coating dental applications. Regarding trabecular bone replacement, this type of bone typically exhibits strengths in the range of 2–12 MPa [53] and Vickers hardness ranging from 0.3246 to 0.4413 GPa [54]. Our research indicates that the compressive strength observed in C_600 samples is 13.58 ± 2.92 MPa, with a Vickers hardness of 0.46 ± 0.09 GPa, further suggesting their potential application in trabecular bone replacement. The higher compressive strength and Vickers hardness observed in samples calcined at higher temperatures indicate their potential for trabecular bone replacement as well as applications in both non-loading and load-bearing sites [53].

4. Conclusions

This work elucidates the intricate composition and mechanical characteristics of fishbone-derived calcium phosphates (CaPs) prepared via a two-step heat treatment. We employed various analytical techniques, such as FTIR spectroscopy, XRD, SEM, and EXAFS analysis, to assess the structural complexities, microstructures, and mechanical properties of the CaPs. Our results revealed variations in the phase concentration, local structure, and microstructure of calcined and sintered CaP samples derived from fish bones depending on the calcination temperature. Through our analysis, the presence of HAp and CHAp was confirmed, with an increased concentration of β-MgTCP at higher temperatures. The sintered samples exhibited larger crystallite sizes, improved crystallinity, and a higher concentration of β-TCP than their corresponding powders. EXAFS results provided insights into the substitution of Mg at the Ca2H, Ca2β, and Ca5β sites. SEM analysis revealed consistent grain sizes, whereas higher calcination temperatures resulted in denser ceramics with fewer pores. Furthermore, the compressive strength and Vickers hardness of the sintered ceramics were observed increased with an increasing calcination temperature. This observation led us to attribute the observed enhancement in mechanical properties primarily to the lower porosity and higher relative density of the sintered ceramics calcined at higher temperatures. The compressive strength and Vickers hardness with values of 54.37 ± 7.61 MPa and 2.92 ± 0.37 GPa, respectively, were observed in the case of the C_900 ceramic. In summary, our study provides a comprehensive understanding of the influence of calcination temperature on the complex nature, unique characteristics, and mechanical properties of fishbone-derived CaPs. While the relatively good mechanical properties observed in these CaP ceramics suggest their suitability for biocompatible dental and trabecular bone replacement applications, further studies, such as brittleness measurements, are necessary to fully assess their performance and durability.

Data availability

Researchers interested in more in-depth information or additional data relating to any segment of the current study are encouraged to contact the corresponding author. We are readily willing to furnish any requested data to contribute to the advancement of scientific understanding in this field.

Ethics declarations

The Nile tilapia (*Oreochromis niloticus*) bones used in this study were obtained as a by-product from a local fish market in the northeast of Thailand. The waste materials were sourced responsibly, considering the environmental impact, and ensuring fair treatment of stakeholders involved in their collection.

CRediT authorship contribution statement

Tanachat Eknapakul: Writing – original draft, Visualization, Validation, Investigation, Conceptualization. **Arreerat Jiamprasertboon:** Investigation, Formal analysis. **Penphitcha Amonpattaratkit:** Formal analysis, Data curation. **Adulphan Pimsawat:** Methodology, Investigation, Data curation. **Sujittra Daengsakul:** Resources, Formal analysis. **Nantawat Tanapongpisit:** Formal analysis, Data curation. **Wittawat Saenrang:** Investigation, Formal analysis. **Atipong Bootchanont:** Validation, Investigation, Formal analysis, Conceptualization. **Pattarapong Wannapraphai:** Formal analysis, Data curation. **Thanawat Phetrattanarangsi:** Formal analysis, Data curation. **Thanachai Boonchuduang:** Formal analysis, Data curation. **Atchara Khamkongkaeo:** Writing – review & editing, Visualization, Validation, Methodology, Investigation, Conceptualization. **Rattikorn Yimnirun:** Supervision, Funding acquisition.

Declaration of competing interest

The authors declare that they have no known competing financial interests or personal relationships that could have appeared to influence the work reported in this paper.

Acknowledgments

References

[1] S. Batool, U. Liaqat, Z. Hussain, M. Sohail, Synthesis, characterization and process optimization of bone whitlockite, Nanomaterials 10 (2020) 1856, https://doi.org/10.3390/nano10091856.

[2] H.L. Jang, K. Jin, J. Lee, Y. Kim, S.H. Nahm, K.S. Hong, K.T. Nam, Revisiting whitlockite, the second most abundant biomineral in bone: nanocrystal synthesis in physiologically relevant conditions and biocompatibility evaluation, ACS Nano 8 (2014) 634–641, https://doi.org/10.1021/nn405246h.

[3] A. Ressler, A. Žužić, I. Ivanišević, N. Kamboj, H. Ivanković, Ionic substituted hydroxyapatite for bone regeneration applications: a review, Open Ceram 6 (2021), https://doi.org/10.1016/j.oceram.2021.100122.

[4] T. Goto, K. Sasaki, Effects of trace elements in fish bones on crystal characteristics of hydroxyapatite obtained by calcination, Ceram. Int. 40 (2014) 10777–10785, https://doi.org/10.1016/j.ceramint.2014.03.067.

[5] P.E. Wang, T.K. Chaki, Sintering behaviour and mechanical properties of hydroxyapatite and dicalcium phosphate, J. Mater. Sci. Mater. Med. 4 (1993) 150–158, https://doi.org/10.1007/BF00120384.

[6] H.-Y. Mi, X. Jing, M.R. Salick, T.M. Cordie, X.-F. Peng, L.-S. Turng, Morphology, mechanical properties, and mineralization of rigid thermoplastic polyurethane/hydroxyapatite scaffolds for bone tissue applications: effects of fabrication approaches and hydroxyapatite size, J. Mater. Sci. 49 (2014) 2324–2337, https://doi.org/10.1007/s10853-013-7931-3.

[7] J. Ran, P. Jiang, G. Sun, Z. Ma, J. Hu, X. Shen, H. Tong, Comparisons among Mg, Zn, Sr, and Si doped nano-hydroxyapatite/chitosan composites for load-bearing bone tissue engineering applications, Mater. Chem. Front. 1 (2017) 900–910, https://doi.org/10.1039/C6QM00192K.

[8] S. Ramesh, K.L. Aw, R. Tolouei, M. Amiriyan, C.Y. Tan, M. Hamdi, J. Purbolaksono, M.A. Hassan, W.D. Teng, Sintering properties of hydroxyapatite powders prepared using different methods, Ceram. Int. 39 (2013) 111–119, https://doi.org/10.1016/j.ceramint.2012.05.103.

[9] L. Duta, G. Dorcioman, V. Grumezescu, A review on biphasic calcium phosphate materials derived from fish discards, Nanomaterials 11 (2021) 2856, https://doi.org/10.3390/nano11112856.

[10] J. Jeong, J.H. Kim, J.H. Shim, N.S. Hwang, C.Y. Heo, Bioactive calcium phosphate materials and applications in bone regeneration, Biomater. Res. 23 (2019) 4, https://doi.org/10.1186/s40824-018-0149-3.

[11] X. Cao, J. Zhu, C. Zhang, J. Xian, M. Li, S. Nath Varma, Z. Qin, Q. Deng, X. Zhang, W. Yang, C. Liu, Magnesium-rich calcium phosphate derived from Tilapia bone has superior osteogenic potential, J. Funct. Biomater. 14 (2023) 390, https://doi.org/10.3390/jfb14070390.

[12] R.G. Carrodeguas, S. De Aza, α-Tricalcium phosphate: synthesis, properties and biomedical applications, Acta Biomater. 7 (2011) 3536–3546, https://doi.org/10.1016/j.actbio.2011.06.019.

[13] H.-S. Ryu, H.-J. Youn, B.-S. Chang, C.-K. Lee, S.-S. Chung, An improvement in sintering property of β-tricalcium phosphate by addition of calcium pyrophosphate, Biomater 23 (2002) 909–914, https://doi.org/10.1016/S0142-9612(01)00201-0.

[14] C. Stähli, A.J. Salinas, N. Döbelin, A. Testino, M. Bohner, Density and phase-purity of α-TCP obtained by sintering of nano-crystalline powder, Ceram. Int. 50 (2024) 8586–8593, https://doi.org/10.1016/j.ceramint.2023.07.068.

[15] K. Salma-Ancane, L. Stipniece, A. Putnins, L. Berzina-Cimdina, Development of Mg-containing porous β-tricalcium phosphate scaffolds for bone repair, Ceram. Int. 41 (2015) 4996–5004, https://doi.org/10.1016/j.ceramint.2014.12.065.

[16] X. Zhang, F. Jiang, T. Groth, K.S. Vecchio, Preparation, characterization and mechanical performance of dense β-TCP ceramics with/without magnesium substitution, J. Mater. Sci. Mater. Med. 19 (2008) 3063–3070, https://doi.org/10.3390/nano11112856.

[17] A. Khamkongkaeo, T. Boonchuduang, W. Klysubun, P. Amonpattaratkit, H.t. Chunate, N. Tuchinda, A. Pimsawat, S. Daengsakul, P. Suksangrat, W. Sailuam, D. Vongpramate, A. Bootchanont, B. Lohwongwatana, Sintering behavior and mechanical properties of hydroxyapatite ceramics prepared from Nile Tilapia (*Oreochromis niloticus*) bone and commercial powder for biomedical applications, Ceram. Int. 47 (2021) 34575–34584, https://doi.org/10.1016/j.ceramint.2021.08.372.

[18] S. Ramesh, Z.Z. Loo, C.Y. Tan, W.J.K. Chew, Y.C. Ching, F. Tarlochan, H. Chandran, S. Krishnasamy, L.T. Bang, A.A.D. Sarhan, Characterization of biogenic hydroxyapatite derived from animal bones for biomedical applications, Ceram. Int. 44 (2018) 10525–10530, https://doi.org/10.1016/j.ceramint.2018.03.072.

[19] O.G. Agbabiaka, I.O. Oladele, A.D. Akinwekomi, A.A. Adediran, A.O. Balogun, O.G. Olasunkanm, T.M.A. Olayanju, Effect of calcination temperature on hydroxyapatite developed from waste poultry eggshell, Sci. Afr. 8 (2020), https://doi.org/10.1016/j.sciaf.2020.e00452.

[20] A. Sobczak, A. Kida, Z. Kowalski, Z. Wzorek, Evaluation of the biomedical properties of hydroxyapatite obtained from bone waste, Pol. J. Chem. Technol. 11 (2009) 37–43, https://doi.org/10.2478/v10026-009-0010-5.

[21] D.H. Butler, R. Shahack-Gross, Formation of biphasic hydroxylapatite-beta magnesium tricalcium phosphate in heat treated salmonid vertebrae, Sci. Rep. 7 (2017) 3610, https://doi.org/10.1038/s41598-017-03737-2.

[22] D. Pham Minh, A. Nzihou, P. Sharrock, Carbonated hydroxyapatite starting from calcite and different orthophosphates under moderate hydrothermal conditions: synthesis and surface reactivity in simulated body fluid, Mater. Res. Bull. 60 (2014) 292–299, https://doi.org/10.1016/j.materresbull.2014.08.052.

[23] J.C. Merry, I.R. Gibson, S.M. Best, W. Bonfield, Synthesis and characterization of carbonate hydroxyapatite, J. Mater. Sci. Mater. Med. 9 (1998) 779–783, https://doi.org/10.1023/A:1008975507498.

[24] I.S. Neira, Y.V. Kolen'ko, O.I. Lebedev, G. Van Tendeloo, H.S. Gupta, F. Guitián, M. Yoshimura, An effective morphology control of hydroxyapatite crystals via hydrothermal synthesis, crys, Growth Des 9 (2009) 466–474, https://doi.org/10.1021/cg800738a.

[25] F. Capitelli, F. Bosi, S.C. Capelli, F. Radica, G. Della Ventura, Neutron and XRD single-crystal diffraction study and vibrational properties of whitlockite, the natural counterpart of synthetic tricalcium phosphate, Crystals 11 (2021) 225, https://doi.org/10.3390/cryst11030225.

[26] T. Kono, T. Sakae, H. Nakada, T. Kaneda, H. Okada, Confusion between carbonate apatite and biological apatite (carbonated hydroxyapatite) in bone and teeth, Minerals 12 (2022) 170, https://doi.org/10.3390/min12020170.

[27] H.E. Pankaew P, Li, P. msuwan, K. Naemchanthara, Temperature effect on calcium phosphate synthesized from chicken eggshells and ammonium phosphate, J. Appl. Sci. 10 (2010) 3337–3342, https://doi.org/10.3923/jas.2010.3337.3342.

[28] M.Z.A. Khiri, K.A. Matori, M.H.M. Zaid, C.A.C. Abdullah, N. Zainuddin, I.M. Alibe, N.A.A. Rahman, S.A.A. Wahab, A.Z.K. Azman, N. Effendy, Crystallization behavior of low-cost biphasic hydroxyapatite/β-tricalcium phosphate ceramic at high sintering temperatures derived from high potential calcium waste sources, Results Phys. 12 (2019) 638–644, https://doi.org/10.1016/j.rinp.2018.12.025.

[29] G. Kresse, J. Furthmüller, Efficiency of ab-initio total energy calculations for metals and semiconductors using a plane-wave basis set, Comput. Mater. Sci. 6 (1996) 15–50, https://doi.org/10.1016/0927-0256(96)00008-0.

[30] J.P. Perdew, A. Zunger, Self-interaction correction to density-functional approximations for many-electron systems, Phys. Rev. B 23 (1981) 5048–5079, https://doi.org/10.1016/0927-0256(96)00008-0.

[31] J.P. Perdew, K. Burke, M. Ernzerhof, Generalized gradient approximation made simple, Phys. Rev. Lett. 77 (1996) 3865–3868, https://doi.org/10.1103/PhysRevLett.77.3865.

[32] H.J. Monkhorst, J.D. Pack, Special points for Brillouin-zone integrations, Phys. Rev. B 13 (1976) 5188–5192, https://doi.org/10.1103/PhysRevB.13.5188.

[33] J.J. Rehr, R.C. Albers, Theoretical approaches to x-ray absorption fine structure, Rev. Mod. Phys. 72 (2000) 621–654, https://doi.org/10.1103/RevModPhys.72.621.

[34] L. Hedin, B.I. Lundqvist, Explicit local exchange-correlation potentials, J. Phys. C Solid State Phys. 4 (1971) 2064, https://doi.org/10.1088/0022-3719/4/14/022.

[35] A.N.K.A. Fara, G. Pragash, H.Z. Abdullah, Effect of calcination on the properties of hydroxyapatite from Tilapia fish bones, Adv. Mater. Res. 1125 (2015) 474–478, https://doi.org/10.4028/www.scientific.net/AMR.1125.474.

[36] H. Pan, B.W. Darvell, Effect of carbonate on hydroxyapatite solubility, Cryst. Growth Des. 10 (2010) 845–850, https://doi.org/10.1021/cg901199h.

[37] K. Nahar U, S B, R. Chandra D, S. Chandra P, S. B, M. Ym, S. Islam Md, Characterization of beta-tricalcium phosphate (β- TCP) produced at different process conditions, J. Bioeng Biomed. Sci. (2017) 7, https://doi.org/10.4172/2155-9538.1000221.

[38] S. Laasri, M. Taha, E.K. Hlil, A. Laghzizil, A. Hajjaji, Manufacturing and mechanical properties of calcium phosphate biomaterials, C. R. Méc. 340 (2012) 715–720, https://doi.org/10.1016/j.crme.2012.09.005.

[39] E. Garskaite, K.-A. Gross, S.-W. Yang, T.C.-K. Yang, J.-C. Yang, A. Kareiva, Effect of processing conditions on the crystallinity and structure of carbonated calcium hydroxyapatite (CHAp), CrystEngComm 16 (2014) 3950–3959, https://doi.org/10.1039/C4CE00119B.

[40] R. Gopal, C. Calvo, Structural relationship of whitlockite and βCa₃(PO₄)₂, Nat. Phys. Sci. (Lond.) 237 (1972) 30–32, https://doi.org/10.1038/physci237030a0.

[41] F. Sharifianjazi, A. Esmaeilkhanian, M. Moradi, A. Pakseresht, M.S. Asl, H. Karimi-Maleh, H.W. Jang, M. Shokouhimehr, R.S. Varma, Biocompatibility and mechanical properties of pigeon bone waste extracted natural nano-hydroxyapatite for bone tissue engineering, Mater. Sci. Eng. B 264 (2021) 114950, https://doi.org/10.1016/j.mseb.2020.114950.

[42] A.M. Castillo-Paz, S.M. Londoño-Restrepo, L. Tirado-Mejía, M.A. Mondragón, M.E. Rodríguez-García, Nano to micro size transition of hydroxyapatite in porcine bone during heat treatment with low heating rates, Prog. Nat. Sci. Mater. Int. 30 (2020) 494–501, https://doi.org/10.1016/j.pnsc.2020.06.005.

[43] A. Rajendran, S. Balakrishnan, R. Kulandaivelu, S.N.T.S. Nellaiappan, Multi-element substituted hydroxyapatites: synthesis, structural characteristics and evaluation of their bioactivity, cell viability, and antibacterial activity, J. Sol. Gel Sci. Technol. 86 (2018) 441–458, https://doi.org/10.1007/s10971-018-4634-x.

[44] B. Le Gars Santoni, L. Niggli, G.A. Sblendorio, D.T.L. Alexander, C. Stähli, P. Bowen, N. Döbelin, M. Bohner, Chemically pure β-tricalcium phosphate powders: evidence of two crystal structures, J. Eur. Ceram. Soc. 41 (2021) 1683–1694, https://doi.org/10.1016/j.jeurceramsoc.2020.09.055.

[45] D.H. Yassuda-Mattos, N.M. de Freitas Costa, D.d.S. Tavares, G.V.O. Fernandes, A. Alves, J.M. Granjeiro, G.D. de Almeida Soares, Study of bone repair in rat dental socket after implantation of porous granules of beta-tricalcium phosphate (β-TCP) and magnesium-substituted beta-tricalcium phosphate (β-TCMP), Key Eng. Mater. 493–494 (2012) 263–268, https://doi.org/10.4028/www.scientific.net/KEM.493-494.263.

[46] N.M.F. Costa, D.H. Yassuda, M.S. Sader, G.V.O. Fernandes, G.D.A. Soares, J.M. Granjeiro, Osteogenic effect of tricalcium phosphate substituted by magnesium associated with Genderm® membrane in rat calvarial defect model, Mater. Sci. Eng. C 61 (2016) 63–71, https://doi.org/10.1016/j.msec.2015.12.003.

[47] W. Xue, K. Dahlquist, A. Banerjee, A. Bandyopadhyay, S. Bose, Synthesis and characterization of tricalcium phosphate with Zn and Mg based dopants, J. Mate. Sci. Mater. Med. 19 (2008) 2669–2677, https://doi.org/10.1007/s10856-008-3395-4.

[48] H. Madupalli, B. Pavan, M.M.J. Tecklenburg, Carbonate substitution in the mineral component of bone: discriminating the structural changes, simultaneously imposed by carbonate in A and B sites of apatite, J. Solid State Chem. 255 (2017) 27–35, https://doi.org/10.1016/j.jssc.2017.07.025.

[49] I. Cacciotti, A. Bianco, M. Lombardi, L. Montanaro, Mg-substituted hydroxyapatite nanopowders: synthesis, thermal stability and sintering behaviour, J. Eur. Ceram. Soc. 29 (2009) 2969–2978, https://doi.org/10.1016/j.jeurceramsoc.2009.04.038.

[50] C.-J. Liao, F.-H. Lin, K.-S. Chen, J.-S. Sun, Thermal decomposition and reconstitution of hydroxyapatite in air atmosphere, Biomater 20 (1999) 1807–1813, https://doi.org/10.1016/S0142-9612(99)00076-9.

[51] O. Takahashi, Y. Tamenori, T. Suenaga, T. Ikeda-Fukazawa, J. Matsuno, A. Tsuchiyama, XANES spectra of forsterite in crystal, surface, and amorphous states, AIP Adv. 8 (2018), https://doi.org/10.1063/1.5017245.

[52] K. Chun, H. Choi, J. Lee, Comparison of mechanical property and role between enamel and dentin in the human teeth, J. Dent. Biomech. 5 (2014) 1758736014520809, https://doi.org/10.1177/1758736014555246.

[53] Q. Fu, E. Saiz, M.N. Rahaman, A.P. Tomsia, Toward strong and tough glass and ceramic scaffolds for bone repair, Adv. Funct. Mater. 23 (2013) 5461–5476, https://doi.org/10.1002/adfm.201301121.

[54] E. Dall'Ara, C. Öhman, M. Baleani, M. Viceconti, The effect of tissue condition and applied load on Vickers hardness of human trabecular bone, J. Biomech. 40 (2007) 3267–3270, https://doi.org/10.1016/j.jbiomech.2007.04.007.